Rainbow trapping of acoustic skyrmions with subwavelength gradient metastructure

Wan-Na Chen(陈婉娜)[1], Jia-Yu Zheng(郑家瑜)[1], Jing-Yi Lv(吕静怡)[1],
Lei Wang(汪磊)[1], and Hong-Wei Wu(吴宏伟)[1,2,†]

[1] *School of Mechanics and Photoelectric Physics, Anhui University of Science and Technology, Huainan* 232001*, China*
[2] *Center for Fundamental Physics, Anhui University of Science and Technology, Huainan* 232001*, China*

(Received 17 August 2025; revised manuscript received 1 October 2025; accepted manuscript online 5 November 2025)

Acoustic skyrmions, topological quasiparticles with nontrivial vector configurations promising for data storage and information processing, have been explored in various acoustic metastructures. However, configuring skyrmionic modes with different frequencies at distinct locations of the structure remains challenging. Here, we propose a cylinder metastructure with gradient grooves to realize rainbow trapping for acoustic skyrmions. By theoretical analysis and numerical calculation, we propose a mathematical mapping from three-dimensional (3D) parameter sphere to two-dimensional (2D) vector ring-shaped surface, and a Néel-type skyrmionic mode of velocity field vectors can be stably formed in ring-shaped grooves with uniform depth. With this mapping relation, we construct the binary and gradient groove structures, and demonstrate that the skyrmionic modes can be stationed at different subareas with different groove depths for different working frequencies for enhancing data storage capacity. The rainbow trapping for acoustic skyrmions not only enables high-density storage of broadband acoustic signals but also ensures data integrity and stability in complex acoustic environments, paving the way for partitioned data storage and information processing in advanced acoustic functional devices.

Keywords: acoustic skyrmion, topology, metastructure

PACS: 43.55.+p, 12.39.Dc, 03.65.Vf

DOI: 10.1088/1674-1056/ae1b77 **CSTR:** 32038.14.CPB.ae1b77

1. Introduction

Skyrmions were first proposed by the British physicist Skyrme in 1962 for constructing a physical model in nuclear physics.[1] However, it is rapidly growing and forms a large research field in magnetic materials over the past decade. Various derivatives (including Néel-type skyrmion,[2] Bloch-type skyrmion,[3] anti-type skyrmion,[4] meron,[5–7] and bimeron[8,9]) of magnetic skyrmions have been found and offer many promising applications in high-density data storage and information processing. Moreover, apart from magnetic materials, the special vector field configuration in real space characterized by skyrmionic number has also been spread into other physical branches, such as optical waves,[10,11] acoustic waves,[12–14] elastic waves,[15] and water waves.[16] In the field of optics, light, as an important information carrier, naturally attracts great attention for constructing optical skyrmions with electric/magnetic fields,[10,11] spins,[17,18] Stokes vector,[19,20] and energy flow vectors.[21]

Compared with optical waves with intrinsic transverse polarization, configuring skyrmions in sound waves, as spinless longitudinal waves, remains extremely challenging. Fortunately, recent experiments[22] have demonstrated that the velocity vectors can be tailored in inhomogeneous sound beams or acoustic evanescent waves supported on the metastructure surface. In this context, acoustic skyrmion lattices and localized skyrmions have also been observed in well-designed acoustic metastructures for velocity field vectors.[12,14,23] Furthermore, we also propose an acoustic Mie resonator to generate multitype topological textures including acoustic skyrmions and merons simultaneously.[24] The configuration of acoustic skyrmions will provide unique advantages including low energy consumption, high sensitivity, subwavelength scale, and multifunctionality for storing sound signals similar to magnetic skyrmions.

Recently, to realize inhomogeneous vector distribution, we have proposed a nonlinear mapping relation and constructed contracting and expanding skyrmionic modes corresponding to concave and convex-type gradient structures.[22] In the present work, we will focus on constructing the mapping from the three-dimensional (3D) parameter sphere to the two-dimensional (2D) vector ring-shaped surface, rather than the circular surface. The mapping relation will provide us a pathway for partitioning the acoustic skyrmions with different working frequencies to different subareas on the structure surface by constructing ring-shaped grooves with different groove depths, called skyrmion rainbow trapping, similar to photonic/phononic rainbow trapping.[25,26] It is worthwhile to expect that partitioned acoustic skyrmions will vastly enhance the data storage and information processing capacity for sound signals.

†Corresponding author. E-mail: hwwu@aust.edu.cn

http://iopscience.iop.org/cpb http://cpb.iphy.ac.cn

In this work, we theoretically propose a mathematical mapping relation from 3D parameter sphere to 2D ring-shaped vector distribution, and numerically demonstrate that the velocity-field vectors can flip continuously from inner ring boundary to outside edge along the radial direction on the ring-shaped grooves with uniform depth to form a Néel-type skyrmionic mode. Based on the mapping relation, we construct the binary and gradient groove structures with different groove depths, and the results indicate that the skyrmionic modes with different working frequencies can be stationed at different subareas for enhancing data storage capacity. Particularly, the end reflection of spoof surface acoustic waves (SSAWs) on gradient groove surface is conducive to forming acoustic skyrmionic mode for realizing rainbow trapping effect here, which is usually unwished for conventional rainbow trapping of propagating waves in gradient structure.[27,28] The gradient metastructure possesses the capacity that partitioning the acoustic skyrmions with different working frequencies to different subareas can enhance the function of the data storage and information processing for sound signals.

2. The mapping relationship from 3D parameter sphere to 2D ring-shaped vector distribution

As a start, we first generate the acoustic skyrmion based on the single ring-shaped groove structure as shown in Fig. 1(a). The total height of the structure is $H+H_0$, where H_0 is the 2-mm thickness of the structural solid bottom and H is the 5-cm depth of the groove. The widths of the structural groove and the groove period are $a = 1.5$ mm and $b = 2.5$ mm, respectively. Based on such ring-shaped groove structure, the skyrmionic mode of acoustic velocity field is generated on the surface of the structure in Fig. 1(b). The colors assigned to the structure indicate the distribution of sound pressure fields, while the color vectors above the structure represent the configuration of velocity fields. Besides, the ring-shaped skyrmion maps from a 3D parameterized sphere onto 2D plane, as illustrated in Fig. 1(b); the south pole on the parameter sphere maps onto the inner ring, while the north pole maps onto the outer ring. This results in an overall Néel type skyrmion distribution to accomplish the gradual flip from upward to downward.

We verify that the ring-shaped skyrmion modes are generated by calculating the skyrmion number on the surface of the structure. The skyrmion number can be expressed by

$$S = \frac{1}{4\pi}\iint \boldsymbol{n}\cdot\left(\frac{\partial \boldsymbol{n}}{\partial x}\times\frac{\partial \boldsymbol{n}}{\partial y}\right)\mathrm{d}x\mathrm{d}y. \tag{1}$$

In our model, the acoustic skyrmion number can reflect the topology of a skyrmionic configuration by the velocity field distributions, where $\boldsymbol{n} = \mathrm{Re}(\boldsymbol{v})/|\mathrm{Re}(\boldsymbol{v})|$. Based on the mapping from 3D parameterized sphere to 2D vector field by longitude $\alpha(\varphi)$ and latitude $\beta(\rho)$, the skyrmion number can be separated into additional topological numbers:

$$S = \left(\frac{1}{2}\int_r^R \sin\beta(\rho)\,\mathrm{d}\rho\right)\left(\frac{1}{2\pi}\int_0^{2\pi}\frac{\mathrm{d}\alpha(\varphi)}{\mathrm{d}\varphi}\mathrm{d}\varphi\right) = P\cdot M, \tag{2}$$

where the integer $M = \frac{1}{2\pi}\left[\alpha(\varphi)\right]|_{\varphi=0}^{\varphi=2\pi}$ defines the vorticity, and the integer $P = -\frac{1}{2}\left[\cos\beta(\rho)\right]|_{\rho=r}^{\rho=R}$ defines the polarity. The integration range of P is from the inner radius r_0 to the outer radius R_0, which fits the generating region of the ring-shaped skyrmion mode. Unlike the traditional mapping of Néel-type skyrmion, in this paper the south pole of the parameter sphere is mapped to the inner ring instead of the traditional center of the circle. This mapping helps to realize the partitioned storage of skyrmion modes with different frequencies. In Fig. 1(b), the skyrmion number of ring-shaped skyrmion is calculated to be 1.0343, which closely approaches the theoretical value of 1. Figure 1(c) shows that as the groove depth increases, the eigen-frequency of the first-order skyrmion mode decreases. It can be further demonstrated from the inset of Fig. 1(c) that as the groove depth increases, its dispersion curve deviates further from the air line (the black dashed line) and the corresponding cutoff frequency at that depth decreases.

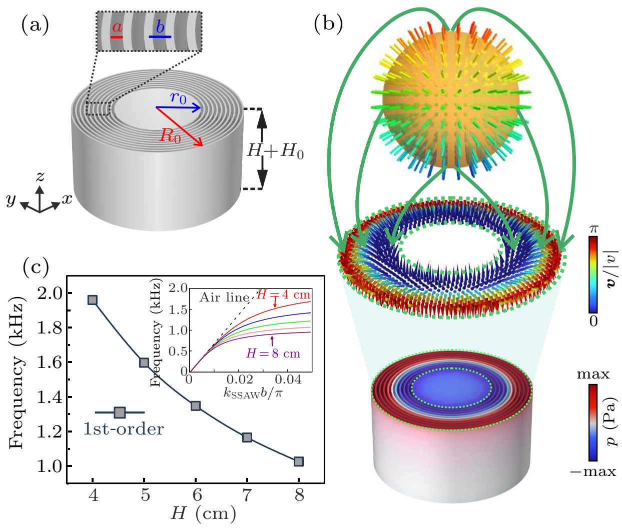

Fig. 1. Schematic structure and simulation results of skyrmion mode on the surface of the single ring-shaped groove structure. (a) Three-dimensional single ring-shaped groove structure schematic, where the inner radius is $r_0 = 2.5$ cm and the outer radius is $R_0 = 5$ cm. (b) Simulation diagram of the skyrmion mode formed by the acoustic velocity field, which maps from 3D parametric sphere to 2D real space. (c) The relationship between the groove depth and the frequency of the first-order of skyrmion mode. The inset shows the corresponding dispersion curves for different values of H.

3. Realization of skyrmion modes with binary groove structure

As mentioned before, the frequency of the skyrmion mode excited at different groove depths is different, and thus we utilize this property to excite ring-shaped skyrmion modes in different regions of the ring-shaped binary groove structure. As shown in Fig. 2(a), the structure is divided into two groove regions, where the inner groove (called groove 1) with depth $h_1 = 7$ cm and the outer groove (called groove 2) with depth $h_2 = 5$ cm, and the corresponding frequency at which the ring-shaped skyrmion mode is excited is 1150 Hz and 1587 Hz, respectively. Figures 2(b) and 2(c) depict the distribution of the acoustic pressure field and velocity field of the ring-shaped skyrmion mode at two different depth regions by numerical calculation in the simulation software COMSOL Multiphysics. As can be seen from the figures, the direction of the velocity vector is upward at the inner radius, while the vector direction keeps flipping as the radius increases, and finally goes downward at the edge of this groove.

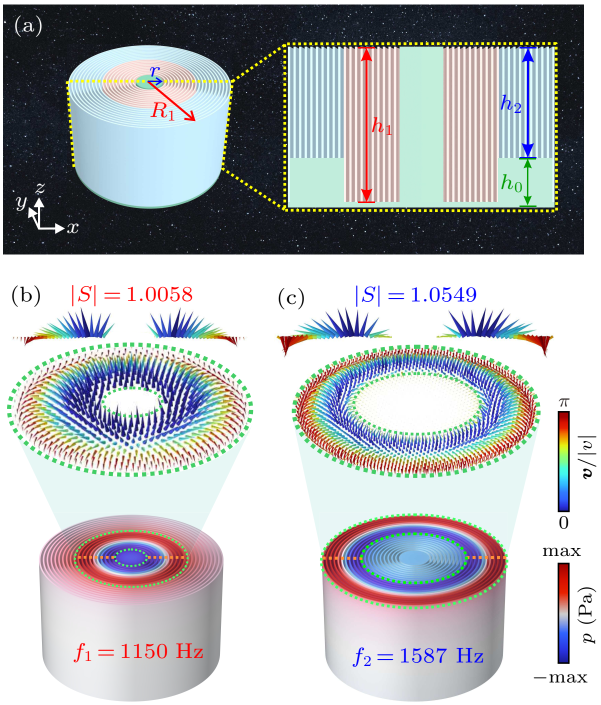

Fig. 2. Schematic structure and simulation results of skyrmion mode on the surface of the ring-shaped binary groove structure. (a) Left: Three-dimensional double ring-shaped groove structure schematic, where the inner radius $r = 1$ cm, the outer radius $R_1 = 6$ cm. Right: Schematic cross-sectional illustration in the z–x plane, where inner groove 1 with depth $h_1 = 7$ cm, outer groove 2 with depth $h_2 = 5$ cm and the blocking height $h_0 = 2.2$ cm. (b) Simulation results of the excitation of a ring-shaped skyrmion at the inner groove 1 with excitation frequency $f_1 = 1150$ Hz. (c) Simulation results of the excitation of a ring-shaped skyrmion at the outer groove 2 with excitation frequency $f_2 = 1587$ Hz. The uppermost acoustic velocity vector distribution is taken from the orange dashed line along the diameter above the structure.

The uppermost arrows in Figs. 2(b) and 2(c) indicate the distribution of the acoustic velocity field vectors on the surface of the structure on line segments taken along the diameter direction, forming a ring-shaped Néel type skyrmion distribution. The difference in size of the downward vectors (red arrows) at the edges of the skyrmion modes is due to the fact that the skyrmion modes generated on groove 1 receive small reflections at the edges and continue diffusing to the groove 2. Thus, the downward vectors at the edges are smaller. In contrast, the skyrmion mode generated on groove 2 receives strong reflections of acoustic waves at the edges of the structure. Thus, the magnitude of the downward vector from the edges of the skyrmion mode is larger. Moreover, we calculate the magnitude of the z-component of velocity field at the edges of the groove 1 and groove 2, finding that the v_z value for groove 1 is smaller than that for groove 2 (5×10^{-4} m/s $< 9 \times 10^{-4}$ m/s), further confirming that the outer boundary of the structure exhibits stronger reflection. Additionally, we also calculate the skyrmion number of the ring-shaped skyrmion modes, and the results are 1.0058 and 1.0549, which are close to the theoretical value of 1, further verifying the production of the ring-shaped skyrmion mode.

4. Realization of rainbow trapping for the skyrmion modes with gradient groove structure

Furthermore, we design a gradient ring-shaped groove structure to realize the rainbow trapping of the skyrmion modes. As illustrated in the line chart above Fig. 3(a), when incident at a certain frequency, the deeper the groove supports the shorter the wavelength of SSAWs, as can be seen from the dispersion curve. Therefore, the sound pressure peaks in this area are sharper. Once the frequency of the surface wave exceeds the cutoff frequency of a certain groove, the surface wave will stop and reflect at the groove; then the reflected wave interferes with the incident wave to form the standing waves constituting the skyrmion modes. Notably, the end reflection of SSAWs on the gradient groove surface is conducive to forming acoustic skyrmionic modes for realizing the rainbow trapping effect here, which is usually unwanted for conventional rainbow trapping of propagating waves in gradient structures.[27,28] These modes satisfy the Fabry–Pérot (FP) resonance condition in the radial direction, which can be expressed as follows:

$$(R - r_n)\, k^n_{\mathrm{SSAW}} = m\pi + \gamma_n, \quad (m = 1, 2, 3, \ldots), \tag{3}$$

where γ_n is the phase shift caused by the edge of the structure in different subareas, and m is an integral index. The specific continuously varying groove distribution is shown in the lower plot of Fig. 3(a). The groove, labeled r_n from the center of the structure, has a corresponding groove depth of h_n, corresponding to the dispersive relation as $k^n_{\mathrm{SSAW}} = k_0\sqrt{1 + \left(\frac{a}{b}\right)^2 \tan^2(k_0 h_n)}$, where k_0 is the wave number of the free space. The relationship between r_n and h_n is shown in the red squares line of Fig. 3(b), which exhibits a linear relationship, with a difference in the depths of adjacent grooves of 0.5 mm. In addition, the frequencies of excited ring-shaped skyrmion modes corresponding to different groove depths are shown as green stars in Fig. 3(b). We selected three frequency points from which the specific ring-shaped skyrmion mode distributions of the sound velocity field are shown in Fig. 3(c).

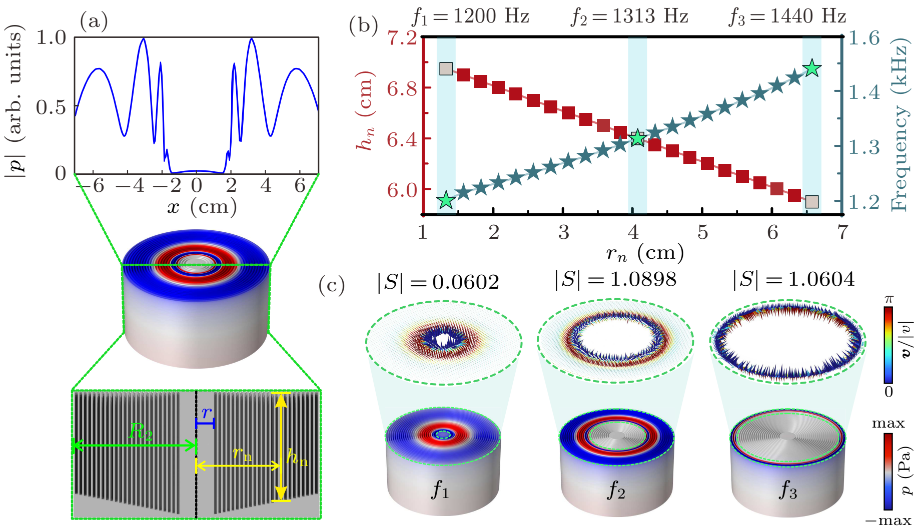

Fig. 3. Schematic diagram of rainbow trapping for the skyrmion modes on the surface of the gradient groove structure. (a) Schematic diagram of rainbow trapping for skyrmion modes with different frequencies can be effectively trapped into different grooves. A schematic cross-section of the structure is shown at the bottom, where the inner radius $r = 1$ cm, the outer radius $R_2 = 7$ cm and the corresponding radius and depth of any groove are r_n and h_n, respectively. (b) The relationship between the groove radius r_n and the groove depth h_n, as well as the relationship between the groove radius r_n and the excitation frequency of the skyrmion mode in the corresponding groove. (c) Simulation diagram of the skyrmion modes formed by the acoustic velocity field in three different excitation frequencies.

As can be seen from Fig. 3(c), the sound pressure distribution on the surface of the structure is not uniform, which is due to the overall downward concave trend of the structural gradient, which causes the skyrmion mode to shrink inward, and the region where the upward vector distribution is located in the inner ring will be smaller than the region where the downward vector distribution is located in the outer ring.[22] We have also calculated the skyrmion number of the skyrmion modes and taken the absolute value at three different frequencies, which were calculated to be 0.0602, 1.0898, and 1.0604, respectively, all of which are close to the theoretical values of 0, 1, and 1. This verifies that the ring-shaped skyrmion modes are generated and trapped efficiently in different regions of the structure.

5. Robustness of rainbow trapping for the skyrmion modes

It is well known that the skyrmion modes are topologically protected against structural deformation and defects. Here, we fabricated two geometrical configurations: a triangular structure (Fig. 4(a)) and a square structure (Fig. 4(b)). Both structures are composed of gradient grooves that remain stable under geometric variations. These structures can also form Néel-type skyrmion modes without affecting the velocity field vector distribution. We selected three different frequency points to verify the robustness and universality of the skyrmion modes. Moreover, the calculated skyrmion number further verifies the protection of this topological quasiparticle under structural deformations.

Furthermore, to verify the robustness of the skyrmionic mode of the acoustic velocity field, we place a long-shaped defect (length × width = 56 mm × 4 mm) along the radius of the structure to block the grooves, as shown in Fig. 4(c), where the defects disrupt the continuity of the slits in the structure. We observed that when the defect width increases to 6 mm, the skyrmion mode in the middle layer (1310 Hz) experiences significant perturbation. This occurs because the long-shaped defect spans the entire middle layer, causing greater disturbance and resulting in distortion of the skyrmion mode. In contrast, for the skyrmion modes generated in the inner layer (1210 Hz) and outer layer (1433 Hz), the defect occupies a smaller area, resulting in less disturbance. Therefore, even when the defect width increases to 8 mm, the skyrmion modes in the inner layer and the outer layer manifest only a slight perturbation in the acoustic velocity field near the defect, and the overall skyrmion mode is still retained. The results indicate that the rainbow trapping effect for the skyrmion modes is highly robust, making it immune to structural deformation and defects.

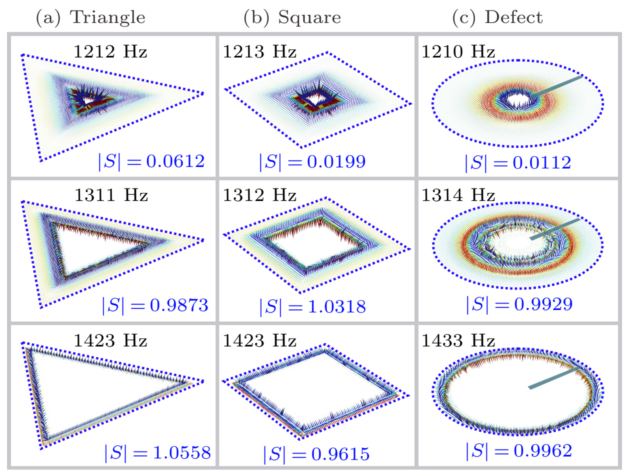

Fig. 4. Robustness of rainbow trapping for the skyrmion modes with different frequencies under structure deformations/defect. (a) and (b) Schematic diagram of rainbow trapping of skyrmion modes under triangular and square structural deformations, respectively. (c) Schematic diagram of rainbow trapping of skyrmion modes under structural defect. The green zones show the location of the defect in velocity field.

6. Conclusion

To summarize, we theoretically propose a mapping relation from a 3D parameter sphere to a 2D ring-shaped vector distribution, rather than the conventionally circular surface, to form a Néel-type skyrmionic mode in the acoustic velocity field. Based on such a mapping relationship in a single groove structure, we further realize the skyrmionic mode of the acoustic velocity field on binary groove and gradient groove structures with different groove depths, respectively. The results indicate that the acoustic skyrmions can be partitioned in different subareas on the structure surface with different working frequencies by constructing ring-shaped grooves with different groove depths. We also demonstrate that the topologically protected skyrmion mode is robust against structure deformations and defects in the gradient groove structure. It is worthwhile to expect that the partitioned acoustic skyrmions may vastly enhance the data storage and information processing capacity for sound signals.

Acknowledgements

Project supported by Scientific Research Projects of Colleges and Universities in Anhui Province, China (Grant No. 2022AH040114) and the Graduate Student Innovation Fund Program of Anhui University of Science and Technology (Grant No. 2024cx2122).

References

[1] Skyrme T H R 1962 *Nucl. Phys.* **31** 556

[2] Kézsmárki I, Bordács S, Milde P, Neuber E, Eng L M, White J S, Rønnow H M, Dewhurst C D, Mochizuki M, Yanai K, Nakamura H, Ehlers D, Tsurkan V and Loidl A 2015 *Nat. Mater.* **14** 1116

[3] Jena J, Göbel B, Ma T, Kumar V, Saha R, Mertig I, Felser C and Parkin S S P 2020 *Nat. Commun.* **11** 1115

[4] Nayak A K, Kumar V, Ma T, Werner P, Pippel E, Sahoo R, Damay F, Rößler U K, Felser C and Parkin S S P 2017 *Nature* **548** 561

[5] Ghosh A, Yang S, Dai Y, Zhou Z, Wang T, Huang C B and Petek H 2021 *Appl. Phys. Rev.* **8** 041413

[6] Lu C, Wang B, Fang X, Tsai D P, Zhu W, Song Q, Deng X, He T, Gong X, Luo H, Wang Z, Dai X, Shi Y and Cheng X 2024 *Nano Lett.* **24** 104

[7] Król M, Sigurdsson H, Rechcińska K, Oliwa P, Tyszka K, Bardyszewski W, Opala A, Matuszewski M, Morawiak P, Mazur R, Piecek W, Kula P, Lagoudakis P G, Piętka B and Szczytko J 2021 *Optica* **8** 255

[8] Desplat L, Kim J V and Stamps R L 2019 *Phys. Rev. B* **99** 174409

[9] Bera S and Mandal S S 2019 *Phys. Rev. Res.* **1** 033109

[10] Tsesses S, Ostrovsky E, Cohen K, Gjonaj B, Lindner N H and Bartal G 2018 *Science* **361** 993

[11] Shen Y, Zhang Q, Shi P, Du L, Yuan X and Zayats A V 2023 *Nat. Photon.* **18** 15

[12] Ge H, Xu X Y, Liu L, Xu R, Lin Z K, Yu S Y, Bao M, Jiang J H, Lu M H and Chen Y F 2021 *Phys. Rev. Lett.* **127** 144502

[13] Muelas-Hurtado R D, Volke-Sepúlveda K, Ealo J L, Nori F, Alonso M A, Bliokh K Y and Brasselet E 2022 *Phys. Rev. Lett.* **129** 204301

[14] Hu P, Wu H W, Sun W J, Zhou N, Chen X, Yang Y Q and Sheng Z Q 2023 *Appl. Phys. Lett.* **122** 022201

[15] Cao L, Wan S, Zeng Y, Zhu Y and Assouar B 2023 *Sci. Adv.* **9** eadf3652

[16] Smirnova D A, Nori F and Bliokh K Y 2024 *Phys. Rev. Lett.* **132** 054003

[17] Zhang Q, Xie Z, Du L, Shi P and Yuan X 2021 *Phys. Rev. Res.* **3** 023109

[18] Zhang Q, Xie Z, Shi P, Yang H, He H, Du L and Yuan X 2022 *Photon. Res.* **10** 947

[19] Tamura R, Kumar P, Rao A S, Tsuda K, Getzlaff F, Miyamoto K, Litchinitser N M and Omatsu T 2024 *APL Photon.* **9** 046104

[20] Cao S, Du L, Shi P and Yuan X 2024 *Opt. Express* **32** 4167

[21] Wang S, Zhou Z, Zheng Z, Sun J, Cao H, Song S, Deng Z L, Qin F, Cao Y and Li X 2024 *Phys. Rev. Lett.* **133** 073802

[22] Sun W J, Wu H W, Hu P, Zhou N, Chen X, Yang Y Q and Sheng Z Q 2023 *Appl. Phys. Lett.* **122** 202201

[23] Zhou N, Chen W N, Sun W J, Sheng Z Q and Wu H W 2024 *Appl. Phys. Lett.* **125** 042204

[24] Chen W N, Wu H W, Lv J Y, Zheng J Y, Zhang W B, Zhou N and Sheng Z Q 2025 *Phys. Rev. B* **111** 174302

[25] Chen S, Qi Y, Li Y, Wang Q and Xiang Y 2024 *Chin. Phys. B* **33** 118701

[26] Lu J Y, Li S F, Li X, Zou X Y and Cheng J C 2025 *Chin. Phys. B* **34** 024302

[27] Gan Q, Ding Y J, Bartoli F J 2009 *Phys. Rev. Lett.* **102** 056801

[28] Zhu J, Chen Y, Zhu X, Garcia-Vidal F J, Yin X, Zhang W and Zhang X 2013 *Sci. Rep.* **3** 1728